Article:

Liu, D., Gu, D., Smyl, D. orcid.org/0000-0002-6730-5277 et al. (2 more authors) (2020) Shape reconstruction using Boolean operations in electrical impedance tomography. IEEE Transactions on Medical Imaging, 39 (9). pp. 2954-2964. ISSN 0278-0062

https://doi.org/10.1109/TMI.2020.2983055

Shape reconstruction using Boolean operations in electrical impedance tomography

Dong Liu, *Member, IEEE*, Danping Gu, Danny Smyl, Jiansong Deng and Jiangfeng Du

***Abstract*— In this work, we propose a new shape reconstruction framework rooted in the concept of Boolean operations for electrical impedance tomography (EIT). Within the framework, the evolution of inclusion shapes and topologies are simultaneously estimated through an explicit boundary description. For this, we use B-spline curves as basic shape primitives for shape reconstruction and topology optimization. The effectiveness of the proposed approach is demonstrated using simulated and experimentally-obtained data (testing EIT lung imaging). In the study, improved preservation of sharp features is observed when employing the proposed approach relative to the recently developed moving morphable components-based approach. In addition, robustness studies of the proposed approach considering background inhomogeneity and differing numbers of B-spline curve control points are performed. It is found that the proposed approach is tolerant to modeling errors caused by background inhomogeneity and is also quite robust to the selection of control points.**

***Index Terms*— Electrical impedance tomography, B-spline curves, Boolean operations, shape reconstruction, lung imaging.**

I. Introduction

ELECTRICAL impedance tomography (EIT) is an imaging modality, which estimates the conductivity distribution within a body from boundary measurements. The invention of EIT as a medical imaging technique is usually attributed to the pioneering work of Webster [1]. The first practical realization of a medical EIT system was detailed in the 1980s by Barber and Brown [2] at the Department of Medical Physics and Clinical Engineering, Royal Hallamshire Hospital in Sheffield (UK). Nowadays, EIT has attracted considerable research interest, and is broadly applicable in the field of medical imaging [3]–[6] and other disciplines such as process tomography [7] and non-destructive testing [8], [9]. For state-of-the-art reviews of EIT, see e.g. [10], [11].

To date, two major categories of EIT reconstruction methods exist, pixel/voxel-based image reconstruction and shape-based image reconstruction. The pixel/voxel-based image reconstruction method is an inverse medium problem using noisy observation data – essentially the estimation of a distribution for the unknown conductivity. Some commonly used inverse methods are the regularized Gauss-Newton method [12], [13], D-bar method [14], subspace-based optimization method [15], nonlinear Land-weber method [16], learning based methods [17]–[19], etc.

Compared to the pixel/voxel-based reconstruction method, shape-based image reconstruction has the advantage of directly incorporating prior information on the target shape into the reconstruction framework; for example, size, location, and the number of inclusions. This feature promotes the ability to reconstruct sharp properties and accurate boundaries. To do this in practice, we formulate the reconstruction problem as an inverse problem using a geometrical representation of embedded objects. Among the shape-based approaches that have been applied are, e.g., factorization methods [20]–[24], linear sampling methods [25], [26], monotonicity-based methods [27]–[30], enclosure based methods [31], [32], shape perturbation method [33], truncated Fourier series [34], [35], direct parameterization methods [36]–[38], geometric constraint methods [39], level set methods [40]–[45], and moving morphable components (MMCs) based method [46].

It is worth noting that in the aforementioned (level set) methods, the inclusion boundary is described in an *implicit* way. For example, in the traditional level set (TLS) methods [40], the level set function (LSF) is usually defined as a signed distance function (SDF). However, the LSF may lose its signed-distance property due to numerical dissipation. Therefore, the LSF is regularly reinitialized, which, in turn, will degrade the robustness and efficiency of the reconstruction.

To achieve better numerical flexibility and computational efficiency, parametric level set (PLS) based methods have been proposed in *absolute* EIT [43], [45], and *difference* EIT [44]. In the PLS scheme, the LSF is decomposed into the weighted summation of radial basis functions (RBFs) defined on each RBF centers. The corresponding weights are chosen as the unknown variables to control the LSF during the reconstruction process. PLS provides a series of benefits for level set based shape reconstruction, including no need for reinitialization and dimension reduction. Concurrently, the clear boundary representation and flexibility in handling topological changes

Manuscript received February 20, 2020; accepted March 21, 2020. This work was supported in part by the National Natural Science Foundation of China (Grants No. 61871356, No. 81788101, No.11771420 and No. 11761131011), in part by the National Key R&D Program of China (Grant No. 2018YFA0306600), in part by the Chinese Academy of Sciences (Grants No. GJJSTD20170001 and No. QYZDY-SSW-SLH004), and in part by the Anhui Initiative in Quantum Information Technologies (Grant No. AHY050000).(Corresponding author: Dong Liu.)

D. Liu and J. Du are with Hefei National Laboratory for Physical Sciences at the Microscale and Department of Modern Physics, University of Science and Technology of China, Hefei 230026, China, also with CAS Key Laboratory of Microscale Magnetic Resonance, University of Science and Technology of China, Hefei 230026, China, and also with Synergetic Innovation Center of Quantum Information and Quantum Physics, University of Science and Technology of China, Hefei 230026, China (e-mail: dong.liu@outlook.com)

D. Gu and J. Deng are with the School of Mathematical Sciences, University of Science and Technology of China, Hefei 230026, China.

D. Smyl is with the Department of Civil and Structural Engineering, University of Sheffield, Sheffield S10 2TN, U.K.

inherited from TLS itself is preserved. However, with RBFs, the corresponding weights have no physical meaning and their ranges cannot be determined explicitly. Further, comparable to TLS, PLS reconstruction regularly shows strong smoothing effects and/or has locally high curvature in the reconstructed shapes, affecting the image quality to the target (to be reconstructed) with sharp properties.

To conduct shape reconstruction in a more geometrically explicit and flexible way, a new shape reconstruction method based on MMCs has been developed for *absolute* EIT [46]. The key idea is to use a set of morphable components represented by hyperelliptic shape and topology description functions (STDFs) with variable parameters (such as lengths, thicknesses, orientations) as the basic blocks of shape reconstruction. Following, the optimal shape is found by optimizing variable parameters in STDFs. It has been shown that this reconstruction method can reduce the number of unknowns substantially and incorporate shape features such as size and location explicitly. However, similar to level set based methods, the reconstruction performance can be influenced by the selection of STDFs. These challenges, and others aforementioned, form the founding motivation for this work.

To address these challenges, we propose a new shape reconstruction framework rooted in Boolean operations, which is inspired from the field of structural topology optimization [47], [48]. Owing to B-spline's local modifiability and flexible controlling property [49], we apply B-spline curves to explicitly describe the boundaries of basic shape primitives which are used to form the shapes in the reconstruction. The proposed framework has the following distinctive features:

- The complex shapes of inclusions are rigorously modeled using Boolean operations coupled with B-spline curves.
- Boolean operations applied to basic shape primitives account for overlapping, merging, and separation of different shapes.
- Shape reconstruction problems are solved through a purely explicit boundary evolution without resorting to hyperelliptic STDFs.
- Direct incorporation of enriching geometric information into the reconstruction.
- The shape reconstruction problem is converted to an inverse problem with a small number of design variables, e.g. the control points of B-spline curves.

To contextualize the proposed framework among contemporaries, Table I provides a comparison of the pros and cons associated with the EIT shape reconstruction approaches.

The article is organized as follows: in Section II, we briefly review the EIT observation model. Following, the properties of explicit boundary representation and the proposed shape reconstruction framework using Boolean operations are introduced in Sections III and IV, respectively. In Section V, we present the implementation details. The numerical and experimental results are shown in Section VI, and a discussion is provided in Section VII. Lastly, conclusions are presented in Section VIII.

II. Forward model of EIT

In EIT, a set of L electrodes (e_ℓ, $\ell = 1, ..., L$) is affixed to the boundary $\partial\Omega$ of a body $\Omega \subset \mathbb{R}^q, q = 2, 3$. The EIT forward problem consists of an electrostatic approximation of Maxwell's equations, and the aim is to compute the electrode voltages U_ℓ (corresponding to electrode e_ℓ) given the injected currents I_ℓ and the conductivity distribution $\sigma(\boldsymbol{x})$, by solving the following partial differential equation

$$\nabla \cdot (\sigma(\boldsymbol{x})\nabla u(\boldsymbol{x})) = 0 \ , \ \boldsymbol{x} \in \Omega, \tag{1}$$

with suitable boundary conditions on $\partial\Omega$. Here $\boldsymbol{x} \in \Omega$ is the spatial coordinate.

Considering the fact that, in medical applications of EIT, contact impedance z_ℓ exists between the skin and electrode e_ℓ, equation (1) is solved together with a set of boundary conditions based on the so-called complete electrode model (CEM) [53]. Specifically, the boundary conditions satisfy

$$u(\boldsymbol{x}) + z_\ell \sigma(\boldsymbol{x}) \frac{\partial u(\boldsymbol{x})}{\partial \nu} = U_\ell, \ \boldsymbol{x} \in e_\ell, \ \ell = 1, ..., L \tag{2}$$

$$\int_{e_\ell} \sigma(\boldsymbol{x}) \frac{\partial u(\boldsymbol{x})}{\partial \nu} \, \mathrm{d}S = I_\ell, \quad \ell = 1, ..., L \tag{3}$$

$$\sigma(\boldsymbol{x}) \frac{\partial u(\boldsymbol{x})}{\partial \nu} = 0, \quad \boldsymbol{x} \in \partial\Omega \backslash \bigcup_{\ell=1}^{L} e_\ell \tag{4}$$

where ν denotes an outward unit normal.

In addition, the current must satisfy the current conversation law and a potential reference level need to be fixed:

$$\sum_{\ell=1}^{L} I_\ell = 0, \quad \sum_{\ell=1}^{L} U_\ell = 0. \tag{5}$$

In this work, we compute the numerical solution to the CEM model (1-5) with finite element method (FEM) (see details in [54]). By assuming an additive noise model for EIT measurement noise, we have the observation model:

$$V = U(\sigma) + \epsilon, \tag{6}$$

where vector V consists all the measurements, $U(\sigma)$ is the FEM based forward solution, and ϵ models the Gaussian distributed noise with mean ϵ^* and covariance matrix Γ_ϵ, which can be experimentally determined, see [55].

III. Explicit boundary representation

In this section, we discuss how to express the shape boundary (inclusion interface) in an explicit way. As an initial effort to develop an explicit boundary evolution-driven shape reconstruction approach, B-spline curves are adopted in the present work to demonstrate the fundamental concept although other types of closed parametric curves may also serve the same purpose.

Let $\mathbf{T} = \{t_0, \cdots, t_m\}$ be a nondecreasing sequence of real numbers, i.e., $t_i \leqslant t_{i+1}, i = 0, \cdots, m-1$. The t_i are called knots, $\mathbf{T}$ is the knot vector and $m+1$ denotes the total number of knots. For brevity, we apply the uniform knot vector †

$$t_i = \frac{i}{m}, \quad i = 0, 1, \ldots, m. \tag{7}$$

†One may also consider to use open uniform and non-uniform knot vector

TABLE I

COMPARISON OF THE PROS AND CONS OF DIFFERENT SHAPE RECONSTRUCTION METHODS IN EIT.

	Name of methods	Pros	Cons
Mathematically justified non-iterative methods	Factorization method [20]–[24]	Upper and lower range bound of conductivity can be treated separately; has a chance to place fewer demands on the data since it only locates an embedded inhomogeneity	Need to know the background conductivity in *a priori*; size estimation of the inclusion is biased; does not give the conductivity value inside the inclusion
	Linear sampling method [25], [26]	Able to handle any number of discrete conductivity values provided the anomalies are separated from each other by the background	Unable to give an indication of the conductivity level but rather locates the jump discontinuities in conductivity; Application to experiment data is still at an early stage
	Monotonicity-based method [27]–[30]	Good performance for detecting convex shapes, and it is often possible to separate inclusions quite well in the presence of noise	For non-convex shapes, one usually gets something that resembles a convex approximation to the shape, either because measurement noise and modeling errors or because of the restricted amount of current patterns; Need to know the background conductivity as *a priori*;
	Enclosure based method [31], [32]	Good performance for detecting convex shapes	Need to know the background conductivity as *a priori*; The performance for non-convex shape estimation is biased; Application to experiment data is still at an early stage
Direct parameterization methods	Shape perturbation method [33]	Direct parameterization for interfacial (close) boundary; Dimension reduction	Need to know the number of inclusions as *a priori*, and hard to handle topological changes; With possibility to be non-convergent; Sensitive to initial guesses
	Fourier series based methods [34], [35]	Direct parameterization for interfacial (close) boundary; Dimension reduction	Need to know the number of inclusions as *a priori*, and hard to handle topological changes; For representing complex shapes, higher order Fourier series have to be used but the coefficients are very sensitive to noise therefore affects the reconstruction performance;
	Front points based method [37], [50], [51]	Direct parameterization for interfacial (open) boundary with discrete front points located on the interface	Only suitable for open interfacial boundary estimation; Need to know the number of phases as *a priori*
	Bézier curve based method [36]	Direct parameterization for interfacial (open) boundary with few control points; Dimension reduction	As a global presentation of shape, it is sensitive to control point movement and cannot represent very complicated shapes; Need to know the number of inclusions/phases as *a priori*
	Geometric constraint method [39]	Capability to incorporate geometric constraints to regularize the reconstruction problem and to automatically exclude the meaningless boundary guesses from the candidate solution	Need to know the number of inclusions as *a priori*, and hard to handle topological changes; Showing strong smoothing effects on sharpness and/or has locally high curvature in the reconstructed shapes
	B-spline curve based methods [38], [52]	Easy to represent the boundary shape with few control points; Capability in preserving sharp properties; Dimension reduction	Need to know the number of inclusions as *a priori*, and hard to handle topological changes;
STDFs-based methods	Traditional level set methods [40], [42]	Flexibility in handling topological changes when phases merges or splits	Need to solve the Hamilton-Jacobi PDE; Need reinitialization
	Parametric level set methods [43]–[45]	Inherit the pros from TLS methods; solve ODEs rather than PDEs;No need for reinitialization; Dimension reduction;	The corresponding weights in RBFs have no physical meaning and their ranges cannot be determined explicitly; Showing strong smoothing effects on sharpness and/or has locally high curvature in the reconstructed shapes
	Hyperelliptic STDF-based MMC method [46]	Inherit the pros from level set based methods; Dimension reduction; Flexibility in incorporating geometric priori information	Shows smoothing effects on sharpness at some extent; the performance will be largely dominant by the selection of STDFs;
	Proposed method using Boolean operations	Inherit the pros from MMC method; Capability in preserving sharp properties; Takes full advantage of B-spline's parametric form for the shape design deformability and flexibility with a few number of design variables, and its implicit form for Boolean operations of the shape primitives accounting for any overlapping, merging and separation of different shape primitives.	B-spline curve may intersect with itself when the control points take some specific values. Cusps will appear on the curve when intersection happens and the detected shape may become too irregular; The calculation of $\frac{\partial \sigma}{\partial \mathcal{P}}$ is based on the perturbation method, which can introduce inaccuracies in the Jacobian computation.

Then, using the Cox-de Boor recursion formula [56], the ith B-spline basis function of degree k (which is set as 3 in this work), denoted by $N_{i,k}(t)$, is recursively defined as

$$N_{i,k}(t) = \frac{t - t_i}{t_{i+k} - t_i} N_{i,k-1}(t) + \frac{t_{i+k+1} - t}{t_{i+k+1} - t_{i+1}} N_{i+1,k-1}(t), \tag{8}$$

$$N_{i,0}(t) = \begin{cases} 1, & t_i \le t < t_{i+1}, \\ 0, & \text{otherwise.} \end{cases} \tag{9}$$

Here, $i = 0, 1, \ldots, n$, $n = m - k - 1$ and n+1 represents the number of B-spline.

Then the B-spline curve can be represented as a linear combination of control points $\{\boldsymbol{p}_i\}_{i=0}^{n}$, namely,

$$\boldsymbol{C}(t) = \sum_{i=0}^{n} N_{i,k}(t) \boldsymbol{p}_i, \tag{10}$$

Next, let's re-write equation (10) in a matrix form

$$\boldsymbol{C} = \boldsymbol{N}\boldsymbol{P}. \tag{11}$$

Here, matrix $\boldsymbol{N} \in \mathbb{R}^{(M+1)\times(n+1)}$ is the matrix composed of B-spline basis functions

$$\boldsymbol{N} = \begin{pmatrix} N_{0,k}(q_0) & N_{1,k}(q_0) & \cdots & N_{n,k}(q_0) \\ N_{0,k}(q_1) & N_{1,k}(q_1) & \cdots & N_{n,k}(q_1) \\ \vdots & \vdots & \ddots & \vdots \\ N_{0,k}(q_M) & N_{1,k}(q_M) & \cdots & N_{n,k}(q_M) \end{pmatrix} \tag{12}$$

where $\{q_i\}_{i=0}^{M}$ is a set of parameter values with $0 \le q_0 < q_1 < \cdots < q_M \le 1$ and M is a positive integer. Matrix $\boldsymbol{P} \in \mathbb{R}^{(n+1)\times 2}$ contains the (unknown) control points, i.e.

$$\boldsymbol{P} = \begin{pmatrix} \boldsymbol{p}_{0,x} & \boldsymbol{p}_{1,x} & \cdots & \boldsymbol{p}_{n,x} \\ \boldsymbol{p}_{0,y} & \boldsymbol{p}_{1,y} & \cdots & \boldsymbol{p}_{n,y} \end{pmatrix}^T. \tag{13}$$

Since we mainly focus on estimating closed boundary shapes, we need to construct a closed B-Spline curve. For this, the most straightforward method to accomplish this is to either use wrapping knot vectors or wrapping control points. In this paper, we utilize the latter to construct closed B-spline curves, i.e., the first k and last k control points need to be wrapped. To this end, we set $\boldsymbol{p}_0 = \boldsymbol{p}_{n-k+1}, \boldsymbol{p}_1 = \boldsymbol{p}_{n-k+2}, \cdots, \boldsymbol{p}_{k-2} = \boldsymbol{p}_{n-1}$ and $\boldsymbol{p}_{k-1} = \boldsymbol{p}_n$.

IV. Shape reconstruction using Boolean operations

In this section, we demonstrate how to represent the geometry of a basic shape primitives in an explicit way and how to perform shape reconstruction and topology optimization using this representation.

Following the common assumption in shape-based reconstruction methods, we begin by assuming that the domain $\Omega \subset \mathbb{R}^2$ contains different regions $\mathcal{F}$ and $\Omega \backslash \mathcal{F}$. Then, we can use a LSF, $f(\boldsymbol{x})$, to represent the shape and topology

$$\begin{cases} f(\boldsymbol{x}) > 0 & \forall \boldsymbol{x} \in \mathcal{F}, \\ f(\boldsymbol{x}) = 0 & \forall \boldsymbol{x} \in \partial\mathcal{F}, \\ f(\boldsymbol{x}) < 0 & \forall \boldsymbol{x} \in \Omega\backslash\mathcal{F}. \end{cases} \tag{14}$$

In this representation, the zero level-set ($f(\boldsymbol{x}) = 0$) refers to the region/inclusion interface. In general terms, the LSF of a topologically complicated region can be constructed through Boolean operations of all LSFs, $\{f_j, j = 1, \cdots, N_c\}$, using the basic shape primitives [47]. In this work, the shape primitives are used for construction of the (unknown) inclusion, and N_c denotes its total number. For example, the Boolean union or intersection of basic shape primitives represented by LSFs can be, respectively, attained by computing their maximum or minimum:

$$\begin{cases} \bigcup_{j=1}^{N_c} f_j = \max_j f_j, \\ \bigcap_{j=1}^{N_c} f_j = \min_j f_j. \end{cases} \tag{15}$$

We remark that other Boolean operations, such as subtraction or difference, can also be used to construct complicated shapes. For the sake of simplicity in presenting the Boolean-based approach proposed in this work, we primarily consider Boolean union in this paper. However, a discussion related to other operations will be addressed in Section VII.

Next, we describe how to use B-spline curves for modeling the shape primitives. For this, we express the basic shape primitives D_j by closed parametric curves, i.e., B-spline based curves $\boldsymbol{C}_j(\boldsymbol{P}^j)$, as shown in Fig. 1. For illustration purposes, we further assume that the background conductivity is σ_0 and there are $N_c = 4$ candidate primitives $D_j, j = 1, \cdots, N_c$ with conductivity profiles as $\sigma(\boldsymbol{x}) = \sigma_1$ for $\boldsymbol{x} \in D_1 \cup D_2$ and $\sigma(\boldsymbol{x}) = \sigma_2$ for $\boldsymbol{x} \in D_3 \cup D_4$ in Ω. Note that the candidate primitives can also be referred to as subregions when they are all disjoint and simply connected. Fig. 1 provides a schematic illustration of the shape and topology modeling realized by means of Boolean operations and B-splines.

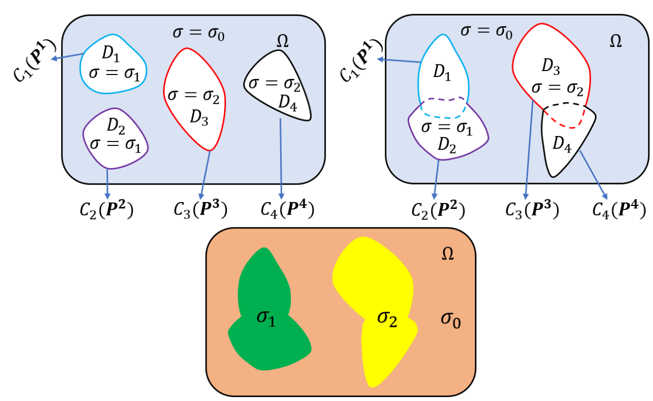

Fig. 1. Shape and topology modeling of the inclusions through Boolean union and B-splines. Top left: initial candidate primitives; Top right: shape and topology modeling with the evolved primitives through Boolean union (dashed lines denote part of the boundary merged into the other primitive); Bottom: one example of conductivity distributions based on the shape and topology shown in top right.

We now recall model (11), where we observe that perturbing the control point vector $\boldsymbol{P}^j$ will result in a change of the closed parametric curve $\boldsymbol{C}_j$. Since the candidate primitives $\boldsymbol{D} = (D_1, D_2, \cdots, D_{N_c})^T$ are determined by the closed parametric curves $\boldsymbol{\mathcal{C}} = (\boldsymbol{C}_1, \boldsymbol{C}_2, \cdots, \boldsymbol{C}_{N_c})^T$, the shape and topology of unknown inclusions are mapped to the space of unknown control points vector $\boldsymbol{\mathcal{P}} = (\boldsymbol{P}^1, \boldsymbol{P}^2, \cdots, \boldsymbol{P}^{N_c})^T$. As a result, the observation model in (6) can be expressed as

$$V = U(\sigma(\boldsymbol{x}, \boldsymbol{\mathcal{P}})) + \epsilon. \tag{16}$$

For sake of straightforwardness, we mainly consider two phase problems in this work, i.e., $\sigma_1 = \sigma_2$. Now, the problem of detecting the unknown inclusions' boundaries and estimating the piecewise constant conductivities σ_0 and σ_1 is equivalent to solving the following minimization problem

$$[\hat{\boldsymbol{\mathcal{P}}}, \hat{\sigma}_0, \hat{\sigma}_1] = \arg\min \Big\{ \|L_\epsilon(V - U(\sigma))\|^2 + \|L_{\boldsymbol{\mathcal{P}}}(\boldsymbol{\mathcal{P}} - \boldsymbol{\mathcal{P}}^*)\|^2 + \|\sigma_0 - \sigma_0^*\|^2 + \|\sigma_1 - \sigma_1^*\|^2 \Big\}. \tag{17}$$

Here, L_ϵ is the Cholesky factor of the inverted noise covariance matrix Γ_ϵ^{-1} (i.e., $L_\epsilon^T L_\epsilon = \Gamma_\epsilon^{-1}$), the regularization matrix $L_{\boldsymbol{\mathcal{P}}}$ is the Cholesky factorization of the matrix $\Gamma_{\boldsymbol{\mathcal{P}}}^{-1}$ (i.e., $L_{\boldsymbol{\mathcal{P}}}^T L_{\boldsymbol{\mathcal{P}}} = \Gamma_p^{-1}$). $\boldsymbol{\mathcal{P}}^*$ is an *a priori* best estimate of $\boldsymbol{\mathcal{P}}$, σ_0^* and σ_1^* are predetermined constant values, see details in Section V-C.

In solving the minimization problem in (17), iterative methods are usually applied. Here, we employ a Gauss-Newton regime equipped with a line-search to compute the optimal step size λ in the solution

$$[\hat{\boldsymbol{\mathcal{P}}}, \hat{\sigma}_0, \hat{\sigma}_1]_{i+1} = [\hat{\boldsymbol{\mathcal{P}}}, \hat{\sigma}_0, \hat{\sigma}_1]_i + \lambda\Delta[\boldsymbol{\mathcal{P}}, \sigma_0, \sigma_1], \tag{18}$$

where $[\hat{\boldsymbol{\mathcal{P}}}, \hat{\sigma}_0, \hat{\sigma}_1]_{i+1}$ denotes the current estimate at iteration $i+1$ and $\Delta[\boldsymbol{\mathcal{P}}, \sigma_0, \sigma_1]$ is the least squares update.

During the iteration, Jacobian term $\boldsymbol{J} = [J_{\boldsymbol{\mathcal{P}}}\ J_{\sigma_0}\ J_{\sigma_1}]$ is required. Applying the chain rule, we have

$$J_{\boldsymbol{\mathcal{P}}} = \frac{\partial U}{\partial \sigma}\frac{\partial \sigma}{\partial \boldsymbol{\mathcal{P}}}, \tag{19}$$

$$J_{\sigma_0} = \frac{\partial U}{\partial \sigma}\frac{\partial \sigma}{\partial \sigma_0}, \tag{20}$$

and

$$J_{\sigma_1} = \frac{\partial U}{\partial \sigma}\frac{\partial \sigma}{\partial \sigma_1}. \tag{21}$$

Here, we apply the standard method [12] to compute $\frac{\partial U}{\partial \sigma}$ and the perturbation method [57] to compute $\frac{\partial \sigma}{\partial \boldsymbol{\mathcal{P}}}$.

In summary, the pseudo code for solving the minimization problem in (17) is given in Algorithm 1.

V. Methods

We begin this section by first describing the construction of LSF and finite element (FE) node characterization, i.e., determining whether a FE node is inside or outside of a primitive. Following, we describe the EIT measurements. Lastly, we address the practical aspects on implementation.

A. Node characterization

In using the proposed approach, a key point is to implicitly characterize the region occupied by the unknown inclusions, which can be easily achieved with the following strategy. Since the boundaries of primitive D_j are explicitly expressed by B-spline curves $\boldsymbol{C}_j$, we can easily use the Inpolygon function in

Algorithm 1 Pseudo code for shape estimation using Boolean operations coupled with B-spline shape primitives.

Initial setting:

1. Set the number of candidate primitives N_c;
2. Set the number of control points $N_p = n + 1$ for each candidate primitives;
3. Set the initial control points vector $\boldsymbol{\mathcal{P}} = (\boldsymbol{P}^1, \boldsymbol{P}^2, \cdots, \boldsymbol{P}^{N_c})^T$;
4. Find the initial candidate primitives $\boldsymbol{D} = (D_1, D_2, \cdots, D_{N_c})^T$ with the use of B-spline curves $\boldsymbol{\mathcal{C}} = (\boldsymbol{C}_1, \boldsymbol{C}_2, \cdots, \boldsymbol{C}_{N_c})^T$ determined by $\boldsymbol{\mathcal{P}}$ and the *Inpolygon* function in Matlab;

Reconstruction:

While Stopping condition not meet **Do**

1.Compute Least square update $\Delta[\boldsymbol{\mathcal{P}}, \sigma_0, \sigma_1] = (\boldsymbol{J}^T L_\epsilon^T L_\epsilon \boldsymbol{J} + blkdiag(L_{\boldsymbol{\mathcal{P}}}^T L_{\boldsymbol{\mathcal{P}}}, 1, 1))^{-1}\boldsymbol{J}^T(V - U(\sigma(\boldsymbol{x}))$;
2. Determining the step-size λ using line search and updating $[\hat{\boldsymbol{\mathcal{P}}}, \hat{\sigma}_0, \hat{\sigma}_1]_{i+1} = [\hat{\boldsymbol{\mathcal{P}}}, \hat{\sigma}_0, \hat{\sigma}_1]_i + \lambda\Delta[\boldsymbol{\mathcal{P}}, \sigma_0, \sigma_1]$;
3. Find the updated primitives $\boldsymbol{D} = (D_1, D_2, \cdots, D_{N_c})^T$ with the use of B-spline curves $\boldsymbol{\mathcal{C}}$ determined by the updated $\hat{\boldsymbol{\mathcal{P}}}_{i+1}$ and the *Inpolygon* function in Matlab;
4. Update the conductivity distribution based on updated primitives $\boldsymbol{D}$ and variables $[\hat{\sigma}_0, \hat{\sigma}_1]_{i+1}$;
5. Calculate the forward problem using the updated $\sigma(\boldsymbol{x})$;
6. Calculate the Jacobian term $\boldsymbol{J} = [\boldsymbol{J}_{\boldsymbol{\mathcal{P}}}\ J_{\sigma_0}\ J_{\sigma_1}]$;

End

MATLAB to test if a FE node (e.g., N_σ) is inside or outside the primitive (see Fig. 2 for reference). If FE node N_σ is inside D_j, then return $\mathbb{IN}(N_\sigma) = 1$ and assign $f_j(N_\sigma) = 1$, otherwise return $\mathbb{IN}(N_\sigma) = 0$ and assign $f_j(N_\sigma) = -1$.

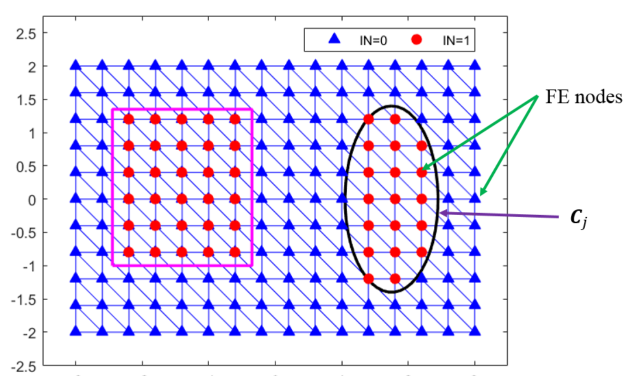

Fig. 2. A schematic illustration of testing whether the FE nodes are inside or outside a primitive.

B. EIT measurements

To demonstrate the efficiency of the proposed approach, we simulated EIT measurements on a circular domain and utilized the experimental data from [43], [46]. In both simulated and experimental studies, $L = 16$ electrodes were equidistantly placed on the target boundary and were applied for use in EIT measurements. Currents with 1 mA amplitude were injected between electrodes i and $j, i = 1, 5, 9, 13$ and $j = 1,., 16\backslash i$, leading to a total number of 54 current patterns. Corresponding to these current injections, 54×16 adjacent electrode potentials were measured. For simulated studies (Cases 1-3), to emulate real-world situations, we added Gaussian noise with the standard deviation 0.1% of the difference between maximum and minimum value of the simulated noiseless voltages to the data. The corresponding signal-noise-ratio is 43 dB.

In the simulations, the conductivity was set as 0.5 mS/cm for inclusions and 2 mS/cm for background, respectively. The inclusions were identified with nested structures, rather than using B-spline curves to represent the boundary of the inclusions. That is, the true values of control points vector $\boldsymbol{\mathcal{P}}$ is not available. In the FEM discretization, due to the presence of different structured inclusions, the numbers of nodes (N_n) and elements (N_e) of the forward meshes in Cases 1-3 were varied, approximately 11500 and 5600, respectively. For the inverse discretization, the numbers of nodes and elements of inverse mesh were fixed at $N_n = 6309$ and $N_e = 3090$. In the experimental studies, the inverse discretization had $N_n = 6309$ and $N_e = 3082$ for Cases 4-6 and $N_n = 7076$ and $N_e = 3413$ for Cases 7&8.

C. Numerical solution aspects

As we mentioned in Section IV, to apply the proposed approach, we need to set the number of control points ($N_p = n+1$) and number of initial candidate primitives (N_c). For this, we set $N_p = 15$, for all the test cases, except the robustness study of the proposed approach *w.r.t* different number of control points in Fig. 7. We remark that the number of duplicated points in the B-spline curve was not included in the number of control points, as mentioned in Section III. Further, we empirically select $N_c = 2$ for Cases 1, 2, 4 & 5. $N_c = 4$ for Cases 3&6 and $N_c = 6$ for Cases 7&8, respectively. For the initial distribution of candidate primitives, see Section VI.

We note that the dimension of unknown parameter $\boldsymbol{\mathcal{P}}$ is proportional to both N_p and N_c, i.e., $\boldsymbol{\mathcal{P}} \in \mathbb{R}^{2 \times N_c \times N_p}$. When selecting N_p and N_c, one should consider the trade-off between ‘reconstruction complexity’ and ‘B-spline’s appearance’. This is because increasing N_p or/and N_c results in an increasingly ill-posed and computationally demanding problem – also, the size of the solution space increases.

It is worth remarking that, the selection of B-spline control points (N_p) and initial candidate primitives (N_c) was done by trial and error and is therefore not optimal. Better selection of both parameters may be conducted by 1) taking into account the relative trade offs with the data discrepancy norm, convergence rate of the minimization problem; 2) incorporating geometric prior information on the target to be reconstructed (e.g., the lung size, shape and location, etc.) and 3) solving the iterative EIT reconstruction problem with a normal pixel-based reconstruction technique and then the (interim) solution could be used to guide the parameter selection to better match the target shape.

Next, the expected value of $\boldsymbol{\mathcal{P}}^*$ was set as the initial guesses, which were selected as 15 equal-angle spaced points along the boundary of initial primitives (simple ellipses used in this paper), since the true value of $\boldsymbol{\mathcal{P}}^*$ is unavailable. Moreover, the regularization matrix $L_{\boldsymbol{\mathcal{P}}}$ was set as the identity matrix. Further, the expected values σ_0^* and σ_1^* were obtained by determining the best homogeneous estimate for σ.

In the reference hyperelliptic STDFs-based reconstruction approach, we follow the implementation details used in [46], i.e., hyperelliptic STDFs with quadratically varying thicknesses were used for expressing the candidate primitives, see details in [46]. Note that, for each test case, to allow an ‘apples-to-apples’ comparison, we use simple ellipses for setting the initial parameters in both proposed and reference methods. That is, the shape and location of initial candidate primitives are the same for both methods.

VI. RESULTS

We begin this section by first showing the results of simulated test Cases 1-3. Following, *high-contrast* (Cases 4-6) and *low-contrast* (Cases 7&8) experimental data are used to further investigate the performance of the proposed approach. Lastly, we demonstrate the primitives’ evolution and provide robustness studies of the proposed approach *w.r.t* different number of control points and modeling errors caused by background inhomogeneity.

The results for different cases are shown in Figs. 3, 4 & 6. In each of these figures, the layouts are the same; meanwhile, the first column shows the ground truth and the second column depicts the initial candidate primitives. Reconstructions based on the refereed hyperelliptic STDFs based approach (marked as ’Hyper ellipse’) and the proposed B-spline approach using Boolean operation (marked as ’Boolean’) are shown in the third and last columns, respectively. Note that, in each of these figures, in order to see the final distribution of primitives, we show the distribution of combined primitives (i.e., the Boolean union of primitives) – in lieu of showing the full conductivity distribution.

Next, to quantitatively access the recovery of piece-wise constant conductivity values and the area of inclusions, we calculated two criteria: the relative contrast (RCo) and the relative coverage ratio (RCR), defined as

$$\mathrm{RCo}\sigma_j = \frac{\widehat{\sigma_j}}{\sigma_j^{\mathrm{True}}}, \quad j = 0, 1, \tag{22}$$

and

$$\mathrm{RCR} = \frac{\text{Estimated inclusion area}}{\text{True inclusion area}}. \tag{23}$$

For both criteria, value 1 would indicate exact match of the true and estimated binary conductivity values or inclusion area, while a value greater or less than 1 would indicate overestimation or underestimation, respectively.

Note that for computing the RCR, half the value of the estimated background conductivity was applied as the threshold for detecting the inclusions, and ImageJ was used to obtain the approximated true areas of the lung-shaped inclusions in Cases 7&8. Also, the RCo values for the inclusions in the experiments were not calculated, since the plastic inclusions in Cases 4-6 are almost non-conductive and the conductivity of lung-shaped inclusions in Cases 7&8 was not measured, given the fact that the conductivity value of agar after solidification cannot be measured using a conductivity meter.

In addition, for the simulated test cases, to analyze the correlation and similarity between the reconstructed image (i.e., the conductivity distribution) and the true image, we also compute the Correlation Coefficient (CC) and the Structural Similarity Index (SSIM) [58]. For reference, the best CC and SSIM values are 1.0 and are achieved when the images are identical, whereby the CC is defined as

$$\mathrm{CC} = \frac{(\sigma_{\text{True}} - \bar{\sigma}_{\text{True}})^{\mathrm{T}}(\mathcal{T}(\sigma(\boldsymbol{x}) - \bar{\sigma}(\boldsymbol{x})))}{\sqrt{||\sigma_{\text{True}} - \bar{\sigma}_{\text{True}}||^2||\sigma(\boldsymbol{x}) - \bar{\sigma}(\boldsymbol{x})||^2}} \times 100\%. \quad (24)$$

where $\mathcal{T}$ is a matrix that interpolates the conductivity $\sigma(\boldsymbol{x})$ from the inverse mesh to the conductivity σ_{True} in the forward mesh and $\bar{\sigma}_{\text{True}}$ and $\bar{\sigma}(\boldsymbol{x})$ are the mean values of σ_{True} and $\sigma(\boldsymbol{x})$, respectively.

A. Reconstructions from simulated data

Fig. 3 depicts the reconstructions of Cases 1-3 using simulated data. We observe that both methods successfully tracked the inclusion positions, size and the basic shape information, leading the criteria close to the true value 1, as tabulated in Table. II. However, by visual inspection, the sharp corners were tracked better with the proposed Boolean-based proposed approach, e.g., the sharp corners of letters 'I' and 'L'-shaped inclusions with the proposed approach were visibly superior to quality of the reference approach. This is an expected result, since the B-spline curves offer an improved ability to preserve sharp properties of the inclusion boundary [38]. On the other hand, the hyperelliptic STDFs in the reference approach lead to smoothed boundaries of the inclusions, which was also observed in [46].

We remark that there is a notable difference between the Boolean-based estimations of the 'T'-shaped inclusion in Cases 2&3. This difference likely results from (a) the increase of ill-posedness in the reconstruction problem, e.g., $\mathcal{P} \in \mathbb{R}^{60}$ in Case 2 relative to $\mathcal{P} \in \mathbb{R}^{120}$ in Case 3, and (b) the presence of 'I'-shaped low conductivity inclusion affected the sensitivity around the 'T'-shaped inclusion.

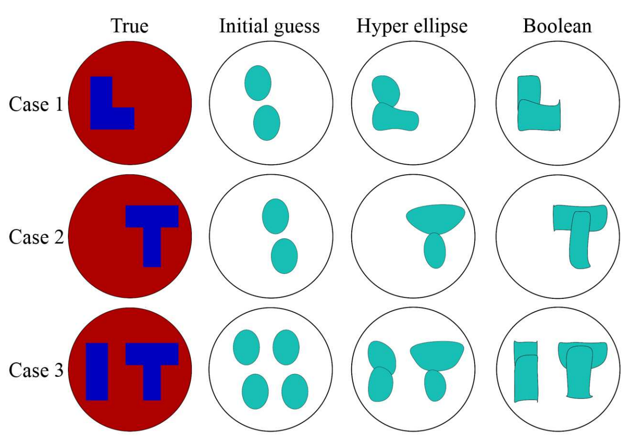

Fig. 3. Cases 1-3: Reconstructions with simulated data.

B. Reconstructions from high-contrast experimental data

In this subsection, we proceed to reconstruct the plastic inclusions in the water tank. Upon immediate visual inspection and comparison of the proposed and reference approaches in Fig. 4, the proposed approach shows better corner reconstruction in the triangle and rectangular-shaped inclusions. On the other hand, the reference approach better reconstructs the circle-shaped inclusion. This is also confirmed by the RCRs shown in Table. III. Once again, this is expected due to the fact that (a) cubic B-spline is known to be unable to exactly represent a circle shape and (b) hyperelliptic STDF has better capability to represent a smoothed boundary.

To illustrate how the primitives evolve during the shape reconstruction process and how the sharp corners/edges of the inclusions form with the Boolean-based approach, we take an example (Case 6) and show the corresponding primitives evolution against the iteration steps, see Fig. 5. For this, we initially applied four primitives (which are more than the number of unknown inclusions in the domain), and let the reconstruction approach automatically morph the shape and topology changes. For example: during the evolution, the two primitives located at the left side of the domain form the shape of rectangle automatically while the other two primitives move to the locations of the triangular and circular inclusion locations. From this figure, we can observe that the proposed approach did not prior information regarding the number of inclusions. This is pragmatically important, since in practical applications we do not always know the number of inclusions (to be estimated) and the shape of unknown inclusion.

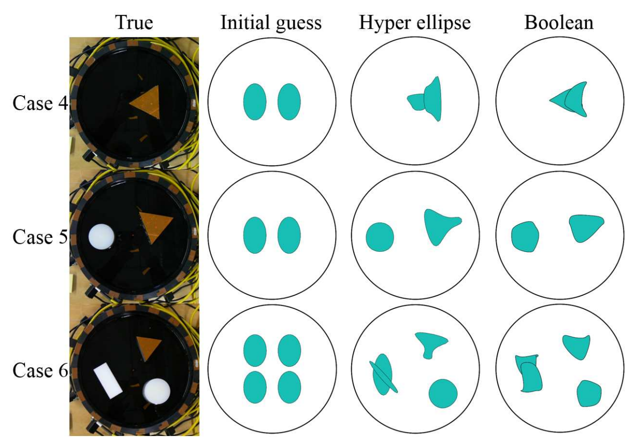

Fig. 4. Cases 4-6: Experimental studies with circular water tank. All the inclusions placed into the water tank are made of plastic materials.

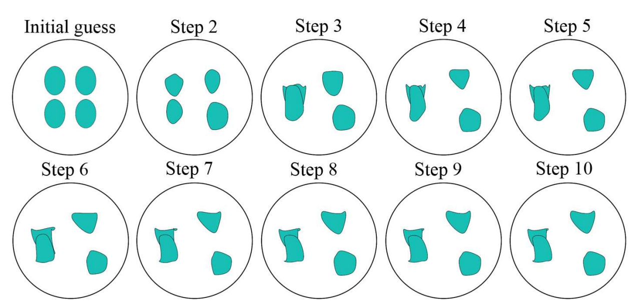

Fig. 5. Primitives evolution during the shape reconstruction in Case 6.

TABLE II
EVALUATION CRITERIA IN SIMULATED TEST CASES: RCOS, RCRS, SSIM AND CC.

	Case 1					Case 2					Case 3					
	RCR	RCoσ_0	RCoσ_1	SSIM	CC	RCR	RCoσ_0	RCoσ_1	SSIM	CC	$\text{RCR}_\text{L}^\dagger$	$\text{RCR}_\text{R}^\dagger$	RCoσ_0	RCoσ_1	SSIM	CC
True	1.00	1.00	1.00	1.00	1.00	1.00	1.00	1.00	1.00	1.00	1.00	1.00	1.00	1.00	1.00	1.00
Hyper ellipse	0.91	0.99	0.94	0.93	0.92	0.97	0.99	0.98	0.93	0.92	1.00	0.93	0.99	0.99	0.90	0.90
Boolean	1.04	0.99	1.00	0.96	0.95	1.08	0.99	1.03	0.95	0.95	1.07	1.04	0.99	1.03	0.91	0.91

† The subscript letters ‘L’ and ‘R’ denote the left and right side inclusions in the measurement domain, respectively.

TABLE III
EVALUATION CRITERIA FOR EXPERIMENTAL STUDIES: RCOS AND RCRS.

	Case 4		Case 5			Case 6				Case 7			Case 8		
	RCR	RCoσ_0	RCR_L	RCR_R	RCoσ_0	$\text{RCR}_\text{r}^\dagger$	$\text{RCR}_\text{t}^\dagger$	$\text{RCR}_\text{c}^\dagger$	RCoσ_0	RCR_L	RCR_R	RCoσ_0	RCR_L	RCR_R	RCoσ_0
True	1.00	1.00	1.00	1.00	1.00	1.00	1.00	1.00	1.00	1.00	1.00	1.00	1.00	1.00	1.00
Hyper ellipse	1.03	0.99	0.92	1.02	1.01	0.95	0.74	0.91	0.99	0.96	0.89	1.00	0.91	0.77	0.99
Boolean	1.03	0.99	1.08	1.00	1.00	1.15	0.97	0.83	0.99	0.87	0.86	0.95	0.90	0.80	0.95

† The subscript letters ‘r’, ‘t’ and ‘c’ under the parameter RCR denote rectangle, triangle and circle-shaped inclusions in the tank, respectively.

C. Reconstructions from low-contrast experimental data

Next, we present the results of Cases 7&8: low-contrast examples within a human thorax-shaped tank, where the lung-shaped inclusions are made of agar. Reconstructions in Fig. 6 clearly show that both approaches generally recover the shapes and locations of the lung-shaped inclusions. However, the lobe parts of both lung-shaped inclusions are better reconstructed by the Boolean-based approach. This behavior reflects the fact that B-spline has the propensity to produce cusps due to a local maximum of curvature produced away from the control points.

Intuitively, upon immediate comparison of Cases 7&8 shown in Fig. 6, the largest visual difference is the disappearance of the heart-shaped inclusion in the reconstructed images of Case 8. This observation is explained by the fact that, (a) comparing to the lung-shaped inclusions, more salt was added into the agar gel for making the heart-shaped inclusion in Case 8, thereby leading a completely different phase compared to the phase of lung-shaped inclusions. (b) as we mentioned in Section IV, we consider two phases problem in this work, so the additional phase will be treated as inhomogeneity in the background, inducing modeling error in the reconstruction. In principle, Case 8 could be considered a robustness study of the proposed approach against the inhomogeneity in the background. Inasmuch, a three phase study with the proposed approach will be discussed in Section VII.

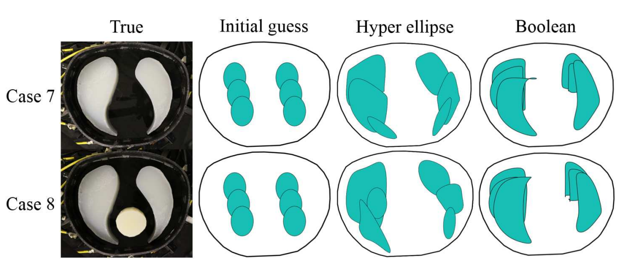

Fig. 6. Cases 7&8: Experimental studies with thorax-shaped tank.

D. Robustness study of the proposed approach against different number of control points

To investigate the robustness of the Boolean-based approach in the presence of varying numbers of control points (N_p) for each primitive, we computed a set of reconstructions for Case 1 with N_p varying from 5 to 20. As shown in Fig. 7, we clearly see that the proposed approach is quite robust to the number of control points, producing reliable reconstructions to the ‘L’-shaped inclusion for most cases. The criteria shown in Fig. 8 supports the feasibility of the proposed approach with varying numbers of control points. However, since the B-spline’s appearance is largely determined by the control points, and consequently its complexity is determined by the number of control points, we suggest not to select too few or too many points, given the reasons in the following (a) when there are too few control points, the B-spline curve may not have enough flexibility to approximate a target curve (i.e., the boundary of complex shape), (b) too many control points may cause redundancy (over-fitting) problem to the approximated target curve, and (c) increasing the number of control points results in an increasingly ill-posed reconstruction problem as the unknowns increase.

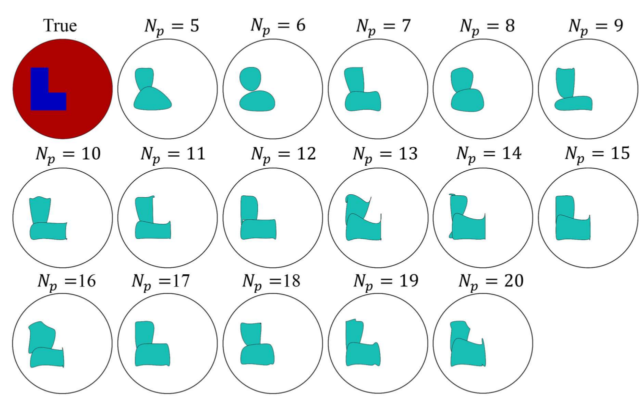

Fig. 7. Robustness study of the proposed approach with respect to different number of control points $\boldsymbol{N_p}$.

It is worth commenting that, in this paper, the initial locations of control points were evenly distributed and the selection of the number of control points was done by trial-and-error and is therefore not optimal. Except the potential strategies mentioned in Section V-C, some other selection methods may be viable by considering automatically adjusting both the locations and number of the initial control points of the B-spline curve [59]. For example, through adding additional new control points or removing redundant control points, one may obtain a B-spline curve with as few control points as possible that approximates a target curve.

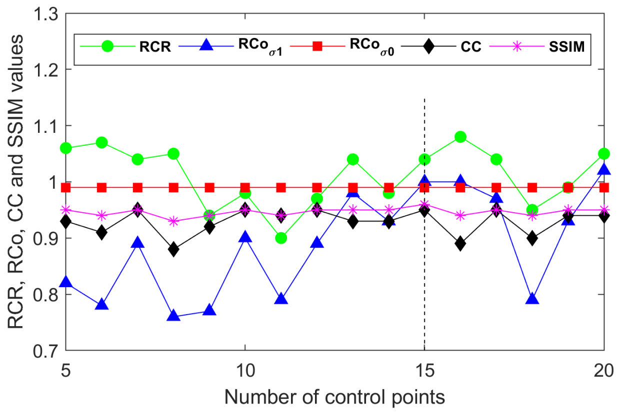

Fig. 8. Evaluation criteria of the robustness study with respect to different number of control points N_p. Dashed line denotes the parameter ($N_p = 15$) used in this paper.

VII. Discussion: Multiphase, current limitations and future work

To this point, the paper has investigated rather simple two phase examples and shown the effectiveness of the Boolean-based approach for recovering inclusions with sharp properties. But, one may ask: can the algorithm handle multiphase and to what extent is the proposed approach still viable?

We begin investigating this query by considering Case 9 in Fig. 9 where the 'T'-shaped inclusion with conductivity $\sigma_1 = 0.5$mS/cm and 'I'-shaped inclusion with conductivity $\sigma_2 = 1$mS/cm, respectively. To do this, we simply extend the formula in (17) as a multiphase estimation problem

$$[\hat{\mathcal{P}}, \hat{\sigma}_0, \hat{\sigma}_1, \hat{\sigma}_2] = \arg\min \left\{ \|L_\epsilon(V - U(\sigma))\|^2 + \|L_{\mathcal{P}}(\mathcal{P} - \mathcal{P}^*)\|^2 + \sum_{j=0}^{2} \|\sigma_j - \sigma_j^*\|^2 \right\}.$$

As demonstrated in Fig. 9, we find that multiple inclusions were accurately localized and the shapes were recognizably reconstructed, which is also evident from the recovery criteria shown on the right hand side. Comparing Case 9 to the test with two phases in Case 3 (see Fig. 3), we clearly see that, in Fig. 9, there is some shape deformation near the boundary occupied by the union of primitives, which is related to (a) the issue of the intersection of two B-spline curves, and (b) comparatively more ill-conditioned multiphase system. For (a), one potential solution is to set the control points located in the other primitives to be inactive (but not removing them) and only retain the control points outside these combined primitives to construct a new B-spline curve [48].

What remains to be discussed is the broader efficacy and limitations of the Boolean-based approach. The present framework is limited by the fact that it is based in the context of absolute imaging, which is known to be sensitive

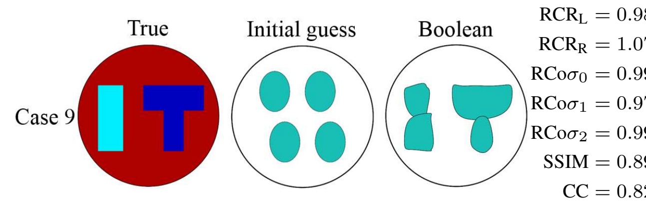

Fig. 9. Multiphase estimation with the proposed approach and the corresponding criteria.

to modeling errors such as inaccuracy in the assumed model geometry. Moreover, absolute imaging is iterative and therefore time consuming. For example, the final reconstructions of 'Boolean' and 'Hyper ellipse' shown in Case 3 were respectively achieved within 10 iterations at average speed of 25 seconds/iteration and 12 iterations at average speed of 20 seconds/iteration, using a desktop PC with an Intel Xeon E3-1231 processor, WD 240 GB SSD and 16GB memory. As such, this framework is not presently intended for on-line monitoring processes. However, two possible solutions for improving the modeling error tolerance ability and speeding up the reconstruction are to (a) formulate the approach in the context of difference imaging, which usually tolerates modeling errors better than traditional absolute imaging and computes reconstructions quickly due to linearization of the forward model, or (b) apply the so-called approximation error method (AEM) [60] to statistically model the errors between an accurate model and a reduced model. These improvements would be crucial for practical medical applications, but less necessary for, e.g., engineering applications that do not require rapid imaging [8].

Lastly, it is intuitively interesting to investigate other types of Boolean operations for shape reconstruction – which can be readily incorporated within the proposed framework. Take, for example, shape reconstruction using a Boolean intersection operation as shown in Fig. 10. In this example, the B-spline curves and the Boolean intersection of two primitives are shown, which form the final reconstruction illustrating the shape and topology of the inclusion. Obviously, the proposed approach with Boolean intersection also works well, producing a very good shape reconstruction of the crescent (confirmed by the reconstruction criteria shown in Fig. 10).

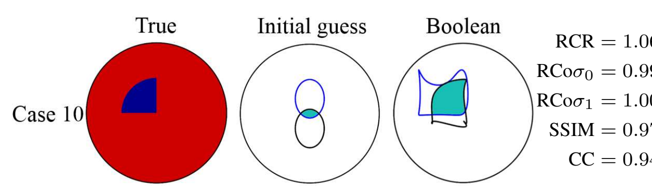

Fig. 10. Shape reconstruction with the proposed approach and Boolean intersection. Solid lines denote the B-spline curves, green patches denote the initial shape (middle) and reconstructed shape (right), respectively, through Boolean intersection of two primitives.

It is worth to remarking here, the article has considered examples with only single Boolean operation. However, in principle, one may consider applying compound Boolean operations, e.g., Boolean union and Boolean subtraction, to form more complicated shapes. For example, when reconstructing lungs with pulmonary nodules, one may use Boolean Union to form the lung shape, and then use Boolean subtraction to locate the pulmonary nodules. Also, similar strategy could be applied to other applications with nested inclusions, e.g., air bubble(s) inside tissue.

In future, we look forward to (i) applying the proposed approach using real medical data, (ii) the broader incorporation of other Boolean operations in the proposed framework, (iii) incooperating the well known active contour model [61] for removing the artifacts on the shape primitives, and (iv) applying tensor product spline surface [56], [62] to track more complicated or multidimensional inclusions. Some remaining challenges to address are centered around mitigating the stringent requirement for accurate knowledge of the domain boundary shape ever-present in absolute imaging and improving the robustness to more complicated conductivity distributions. For this, we look forward to integrating the AEM to the current approach, taking full advantage of shape and topology optimization using Boolean operations and the use of multiple B-spline curves in modeling the conductivity distribution. In addition, we anticipate the proposed framework to be highly applicable to 3D shape reconstruction where the contrast between the number of voxels and the number of control points in the proposed approach is more significant.

VIII. Conclusions

In this paper, we proposed a Boolean-based shape reconstruction framework utilizing B-splines to explicitly describe the evolving boundaries of basic shape primitives. The effectiveness of the proposed approach was demonstrated in a suite of EIT simulation and phantom studies. In the testing campaign, it was shown that sharp features were better preserved when employing the Boolean-based approach than when using the hyperelliptic STDFs-based approach. Moreover, it was found that the proposed approach is tolerant to modeling errors caused by background inhomogeneity and is also quite robust to the selection of differing numbers of control points used to represent the B-spline curves.

Acknowledgment

The authors would like to thank the inverse problems group at University of Eastern Finland, for providing us with the experimental data.

References

[1] R. P. Henderson and J. G. Webster, "An impedance camera for spatially specific measurements of the thorax," *IEEE transactions on bio-medical engineering*, vol. 25, no. 3, pp. 250–4, 1978.

[2] D. C. Barber and B. H. Brown, "Applied potential tomography," *Journal of Physics E: Scientific Instruments*, vol. 17, no. 9, pp. 723–733, sep 1984.

[3] T. Mauri, A. Mercat, and G. Grasselli, "What's new in electrical impedance tomography," *Intensive care medicine*, pp. 1–4, 2018.

[4] J. L. Mueller, P. Muller, M. Mellenthin, R. Murthy, M. Capps, M. Alsaker, R. Deterding, S. D. Sagel, and E. DeBoer, "Estimating regions of air trapping from electrical impedance tomography data," *Physiological measurement*, vol. 39, no. 5, p. 05NT01, 2018.

[5] I. Frerichs, P. A. Dargaville, and P. C. Rimensberger, "Regional pulmonary effects of bronchoalveolar lavage procedure determined by electrical impedance tomography," *Intensive care medicine experimental*, vol. 7, no. 1, p. 11, 2019.

[6] Z. Zhao, M. Y. Chang, M. Y. Chang, C. H. Gow, J. H. Zhang, Y. L. Hsu, I. Frerichs, H. T. Chang, and K. Möller, "Positive end-expiratory pressure titration with electrical impedance tomography and pressure–volume curve in severe acute respiratory distress syndrome," *Annals of Intensive Care*, vol. 9, no. 1, p. 7, 2019.

[7] J. Yao and M. Takei, "Application of process tomography to multiphase flow measurement in industrial and biomedical fields-a review," *IEEE Sensors Journal*, 2017.

[8] D. Smyl, M. Pour-Ghaz, and A. Seppänen, "Detection and reconstruction of complex structural cracking patterns with electrical imaging," *NDT & E International*, vol. 99, pp. 123–133, 2018.

[9] A. Cultrera, D. Serazio, A. Zurutuza, A. Centeno, O. Txoperena, D. Etayo, A. Cordon, A. Redo-Sanchez, I. Arnedo, M. Ortolano, and L. Callegaro, "Mapping the conductivity of graphene with Electrical Resistance Tomography," *Scientific Reports*, vol. 9, no. 1, p. 10655, Dec. 2019.

[10] A. Adler and A. Boyle, "Electrical impedance tomography: Tissue properties to image measures," *IEEE Transactions on Biomedical Engineering*, vol. 64, no. 11, pp. 2494–2504, 2017.

[11] T. de Castro Martins, A. K. Sato, F. S. de Moura, E. D. L. B. de Camargo, O. L. Silva, T. B. R. Santos, Z. Zhao, K. Möeller, M. B. P. Amato, J. L. Mueller *et al.*, "A review of electrical impedance tomography in lung applications: Theory and algorithms for absolute images," *Annual Reviews in Control*, 2019.

[12] M. Vauhkonen, D. Vadasz, P. A. Karjalainen, E. Somersalo, and J. P. Kaipio, "Tikhonov regularization and prior information in electrical impedance tomography," *IEEE transactions on medical imaging*, vol. 17, no. 2, pp. 285–293, 1998.

[13] D. Liu, V. Kolehmainen, S. Siltanen, A.-M. Laukkanen, and A. Seppänen, "Nonlinear difference imaging approach to three-dimensional electrical impedance tomography in the presence of geometric modeling errors," *IEEE Transactions on Biomedical Engineering*, vol. 63, no. 9, pp. 1956–1965, 2016.

[14] S. Siltanen, J. Mueller, and D. Isaacson, "An implementation of the reconstruction algorithm of a nachman for the 2d inverse conductivity problem," *Inverse Problems*, vol. 16, no. 3, p. 681, 2000.

[15] X. Chen, *Computational Methods for Electromagnetic Inverse Scattering*. John Wiley & Sons, 2018.

[16] Z. Cui, W. Qi, X. Qian, W. Fan, L. Zhang, C. Zhang, B. Sun, H. Wang, and W. Yang, "A review on image reconstruction algorithms for electrical capacitance/resistance tomography," *Sensor Review*, vol. 36, no. 4, pp. 429–445, 2016.

[17] S. Liu, J. Jia, Y. D. Zhang, and Y. Yang, "Image reconstruction in electrical impedance tomography based on structure-aware sparse bayesian learning," *IEEE Transactions on Medical Imaging*, vol. 37, no. 9, pp. 2090–2102, 2018.

[18] S. J. Hamilton and A. Hauptmann, "Deep d-bar: Real time electrical impedance tomography imaging with deep neural networks," *IEEE Transactions on Medical Imaging*, vol. 37, no. 10, pp. 2367–2377, 2018.

[19] Z. Wei and X. Chen, "Induced-Current Learning Method for Nonlinear Reconstructions in Electrical Impedance Tomography," *IEEE Transactions on Medical Imaging*, 2019. [Online]. Available: 10.1109/TMI.2019.2948909

[20] M. Brühl and M. Hanke, "Numerical implementation of two noniterative methods for locating inclusions by impedance tomography," *Inverse Problems*, vol. 16, no. 4, pp. 1029–1042, Aug. 2000.

[21] B. Gebauer and N. Hyvönen, "Factorization method and irregular inclusions in electrical impedance tomography," *Inverse Problems*, vol. 23, no. 5, pp. 2159–2170, sep 2007.

[22] B. Harrach, "Recent progress on the factorization method for electrical impedance tomography," *Computational and mathematical methods in medicine*, vol. 2013, 2013.

[23] A. Lechleiter, N. Hyvönen, and H. Hakula, "The factorization method applied to the complete electrode model of impedance tomography," *Siam Journal on Applied Mathematics*, vol. 68, no. 4, pp. 1097–1121, 2008.

[24] N. Chaulet, S. Arridge, T. Betcke, and D. Holder, "The factorization method for three dimensional electrical impedance tomography," *Mathematics*, vol. 30, no. 4, pp. 45 005–45 019(15), 2014.

[25] M. Brühl, "Explicit Characterization of Inclusions in Electrical Impedance Tomography," *SIAM Journal on Mathematical Analysis*, vol. 32, no. 6, pp. 1327–1341, Jan. 2001.

[26] M. Hanke and M. Brühl, "Recent progress in electrical impedance tomography," *Inverse Problems*, vol. 19, no. 6, p. S65, 2003.

[27] B. Harrach and M. Ullrich, "Monotonicity-based shape reconstruction in electrical impedance tomography," *SIAM Journal on Mathematical Analysis*, vol. 45, no. 6, pp. 3382–3403, 2013.

[28] H. Garde and S. Staboulis, "Convergence and regularization for monotonicity-based shape reconstruction in electrical impedance tomography," *Numerische Mathematik*, vol. 135, no. 4, pp. 1–31, 2017.
[29] H. Garde, "Comparison of linear and non-linear monotonicity-based shape reconstruction using exact matrix characterizations," *Inverse Problems in Science and Engineering*, vol. 26, no. 1, pp. 33–50, Jan. 2018.
[30] L. Zhou, B. Harrach, and J. K. Seo, "Monotonicity-based electrical impedance tomography for lung imaging," *Inverse Problems*, vol. 34, no. 4, p. 045005, 2018.
[31] M. Ikehata, "Enclosing a polygonal cavity in a two-dimensional bounded domain from cauchy data," *Inverse Problems*, vol. 15, no. 5, p. 1231, 1999.
[32] ——, "Reconstruction of the support function for inclusion from boundary measurements," *Journal of Inverse and Ill-Posed Problems*, vol. 8, no. 4, pp. 367–378, 2000.
[33] S. Ren, M. Soleimani, Y. Xu, and F. Dong, "Inclusion boundary reconstruction and sensitivity analysis in electrical impedance tomography," *Inverse Problems in Science and Engineering*, vol. 26, no. 7, pp. 1037–1061, 2018.
[34] V. Kolehmainen, S. Arridge, W. Lionheart, M. Vauhkonen, and J. Kaipio, "Recovery of region boundaries of piecewise constant coefficients of an elliptic pde from boundary data," *Inverse Problems*, vol. 15, no. 5, p. 1375, 1999.
[35] A. Rashid, S. Kim, D. Liu, and K. Kim, "A dynamic oppositional biogeography-based optimization approach for time-varying electrical impedance tomography," *Physiological measurement*, vol. 37, no. 6, p. 820, 2016.
[36] O.-P. Tossavainen, M. Vauhkonen, L. Heikkinen, and T. Savolainen, "Estimating shapes and free surfaces with electrical impedance tomography," *Measurement Science and Technology*, vol. 15, no. 7, p. 1402, 2004.
[37] S. Kim, U. Z. Ijaz, A. K. Khambampati, K. Y. Kim, M. C. Kim, and S. I. Chung, "Moving interfacial boundary estimation in stratified flow of two immiscible liquids using electrical resistance tomography," *Measurement Science and Technology*, vol. 18, no. 5, pp. 1257–1269, 2007.
[38] D. Liu, D. Gu, D. Smyl, J. Deng, and J. Du, "B-spline-based sharp feature preserving shape reconstruction approach for electrical impedance tomography," *IEEE transactions on medical imaging*, vol. 38, pp. 2533–2544, 2019.
[39] S. Ren, Y. Wang, G. Liang, and F. Dong, "A robust inclusion boundary reconstructor for electrical impedance tomography with geometric constraints," *IEEE Transactions on Instrumentation and Measurement*, vol. 68, no. 3, pp. 762–773, 2018.
[40] M. Soleimani, W. Lionheart, and O. Dorn, "Level set reconstruction of conductivity and permittivity from boundary electrical measurements using experimental data," *Inverse problems in science and engineering*, vol. 14, no. 2, pp. 193–210, 2006.
[41] P. Rahmati, M. Soleimani, S. Pulletz, I. Frerichs, and A. Adler, "Level-set-based reconstruction algorithm for eit lung images: first clinical results," *Physiological measurement*, vol. 33, no. 5, p. 739, 2012.
[42] D. Liu, A. K. Khambampati, S. Kim, and K. Y. Kim, "Multi-phase flow monitoring with electrical impedance tomography using level set based method," *Nuclear Engineering and Design*, vol. 289, pp. 108–116, 2015.
[43] D. Liu, A. K. Khambampati, and J. Du, "A parametric level set method for electrical impedance tomography," *IEEE Transactions on Medical Imaging*, vol. 37, no. 2, pp. 451–460, 2018.
[44] D. Liu, D. Smyl, and J. Du, "A parametric level set based approach to difference imaging in electrical impedance tomography," *IEEE transactions on medical imaging*, vol. 38, no. 1, pp. 145–155, 2019.
[45] D. Liu, Y. Zhao, A. K. Khambampati, A. Seppanen, and J. Du, "A parametric level set method for imaging multi-phase conductivity using electrical impedance tomography," *IEEE Transactions on Computational Imaging*, vol. 4, no. 4, pp. 552–561, 2018.
[46] D. Liu and J. Du, "A moving morphable components based shape reconstruction framework for electrical impedance tomography," *IEEE transactions on medical imaging*, vol. 38, no. 12, pp. 2937–2948, 2019.
[47] W. Zhang, L. Zhao, T. Gao, and S. Cai, "Topology optimization with closed B-splines and Boolean operations," *Computer Methods in Applied Mechanics and Engineering*, vol. 315, pp. 652–670, Mar. 2017.
[48] W. Zhang, W. Yang, J. Zhou, D. Li, and X. Guo, "Structural topology optimization through explicit boundary evolution," *Journal of Applied Mechanics*, vol. 84, no. 1, p. 011011, 2017.
[49] W. J. Gordon and R. F. Riesenfeld, "B-spline curves and surfaces," in *Computer aided geometric design*. Elsevier, 1974, pp. 95–126.
[50] A. K. Khambampati, Y. J. Hong, K. Y. Kim, and S. Kim, "A boundary element method to estimate the interfacial boundary of two immiscible stratified liquids using electrical resistance tomography," *Chemical Engineering Science*, vol. 95, pp. 161–173, 2013.
[51] A. K. Khambampati, K. Y. Kim, Y.-G. Lee, and S. Kim, "Boundary element method to estimate the time-varying interfacial boundary in horizontal immiscible liquids flow using electrical resistance tomography," *Applied Mathematical Modelling*, vol. 40, no. 2, pp. 1052–1068, 2016.
[52] S. Babaeizadeh and D. H. Brooks, "Electrical impedance tomography for piecewise constant domains using boundary element shape-based inverse solutions," *IEEE transactions on medical imaging*, vol. 26, no. 5, pp. 637–647, 2007.
[53] E. Somersalo, M. Cheney, and D. Isaacson, "Existence and uniqueness for electrode models for electric current computed tomography," *SIAM Journal on Applied Mathematics*, vol. 52, no. 4, pp. 1023–1040, 1992.
[54] P. Vauhkonen, M. Vauhkonen, T. Savolainen, and J. Kaipio, "Three-dimensional electrical impedance tomography based on the complete electrode model," *IEEE Trans. Biomed. Eng*, vol. 46, pp. 1150–1160, 1999.
[55] L. M. Heikkinen, T. Vilhunen, R. M. West, and M. Vauhkonen, "Simultaneous reconstruction of electrode contact impedances and internal electrical properties: Ii. laboratory experiments," *Measurement Science and Technology*, vol. 13, no. 12, p. 1855, 2002.
[56] C. de Boor, *A practical guide to splines*. Springer-verlag New York, 1978, vol. 27.
[57] T. J. Yorkey, J. G. Webster, and W. J. Tompkins, "Comparing reconstruction algorithms for electrical impedance tomography," *IEEE Transactions on Biomedical Engineering*, no. 11, pp. 843–852, 1987.
[58] Z. Wang, A. C. Bovik, H. R. Sheikh, and E. P. Simoncelli, "Image quality assessment: from error visibility to structural similarity," *IEEE transactions on image processing*, vol. 13, no. 4, pp. 600–612, 2004.
[59] H. Yang, W. Wang, and J. Sun, "Control point adjustment for b-spline curve approximation," *Computer-Aided Design*, vol. 36, no. 7, pp. 639–652, 2004.
[60] A. Nissinen, V. P. Kolehmainen, and J. P. Kaipio, "Compensation of modelling errors due to unknown domain boundary in electrical impedance tomography," *IEEE Transactions on Medical Imaging*, vol. 30, no. 2, pp. 231–242, 2011.
[61] M. Kass, A. Witkin, and D. Terzopoulos, "Snakes: Active contour models," *International Journal of Computer Vision*, vol. 1, no. 4, pp. 321–331, 1988. [Online]. Available: https://doi.org/10.1007/BF00133570
[62] D. Liu, D. Gu, D. Smyl, J. Deng, and J. Du, "B-spline level set method for shape reconstruction in electrical impedance tomography," to be published. [Online]. Available: doi:10.1109/TMI.2019.2961938